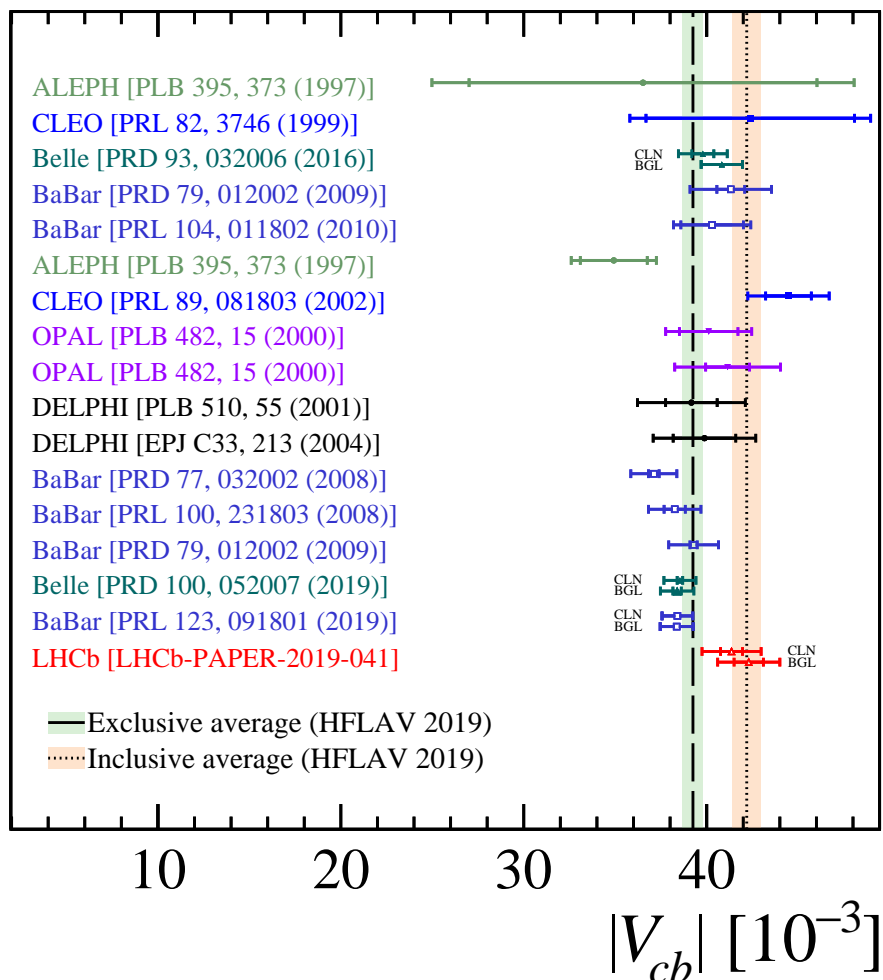# Supplementary material for LHCb-PAPER-2019-041

Figure 1: Summary of all exclusive measurements of $|V_{cb}|$. Error bars show total (outer) and statistical (inner, when present) uncertainties. When not stated, the measurement is obtained using the CLN parametrization. The average of the CLN results does not include the LHCb result, nor that from BaBar [PRL 123, 091801 (2019)]. The average of the inclusive determinations is also reported.
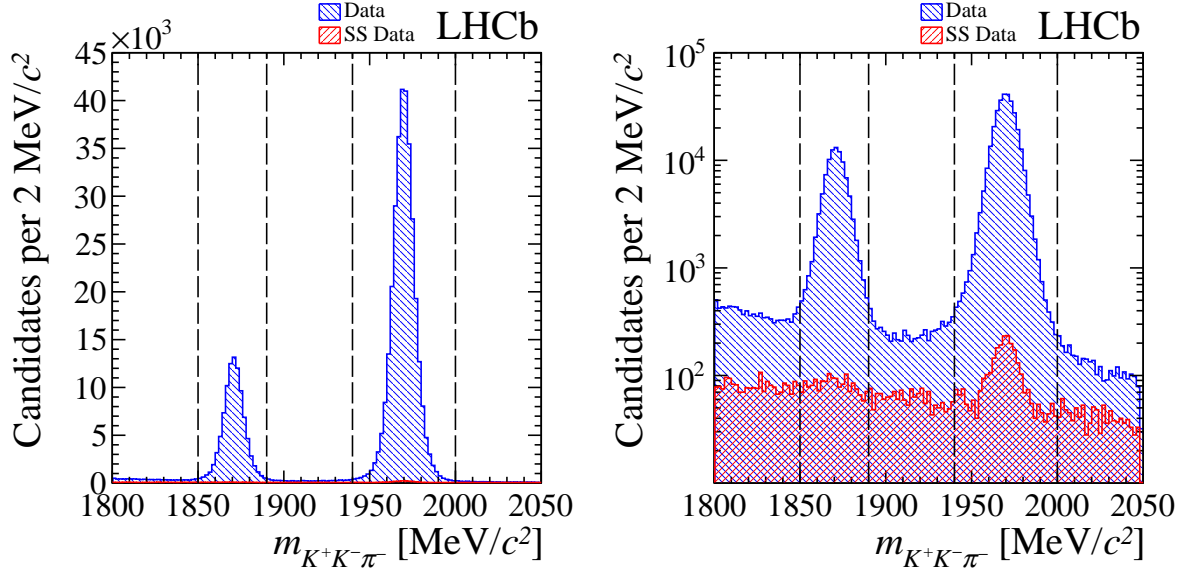
Figure 2: Distributions of $K^+K^-\pi^-$ invariant mass for the selected $D_{(s)}^-\mu^+$ candidates with both (left) linear and (right) logarithmic scales on the y axis. The vertical lines indicate the selected mass ranges.
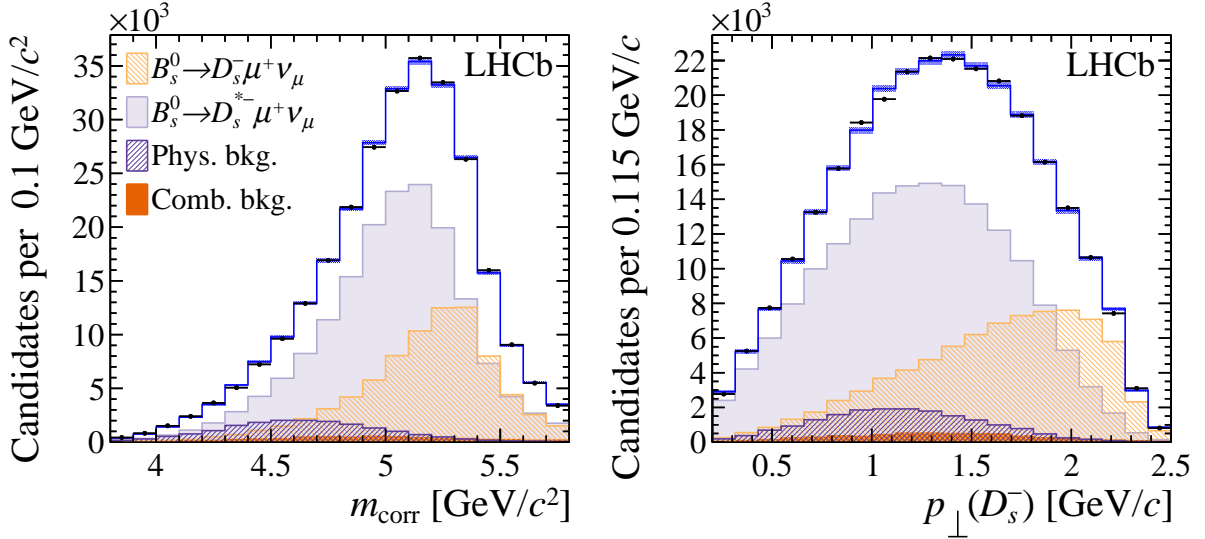

Figure 3: Distribution of (left) m_{corr} and (right) $p_\perp(D_s^-)$ for the inclusive sample of signal $D_s^-\mu^+$ candidates, with BGL fit projections overlaid. The projections of the two components due to physics background are merged together for displaying purposes.
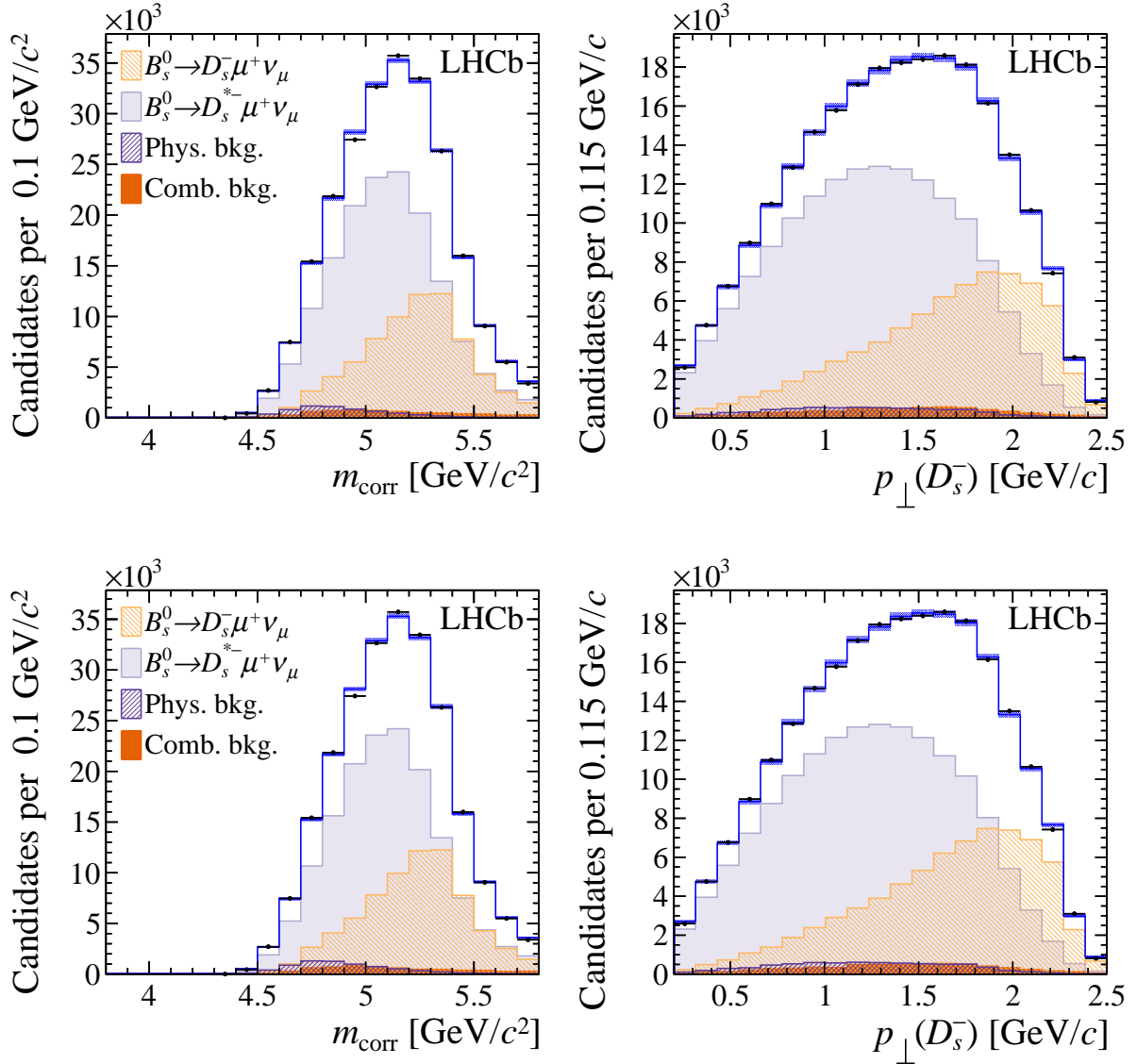
Figure 4: Distribution of (left) m_{corr} and (right) $p_\perp(D_s^-)$ for the inclusive sample of signal $D_s^-\mu^+$ candidates selected with the tighter cut on the m_{corr}–$p_\perp(D_s^-)$ plane, with fit projections based on the (top) CLN and (bottom) BGL parametrizations overlaid. The projections of the two components due to physics background are merged together for displaying purposes.
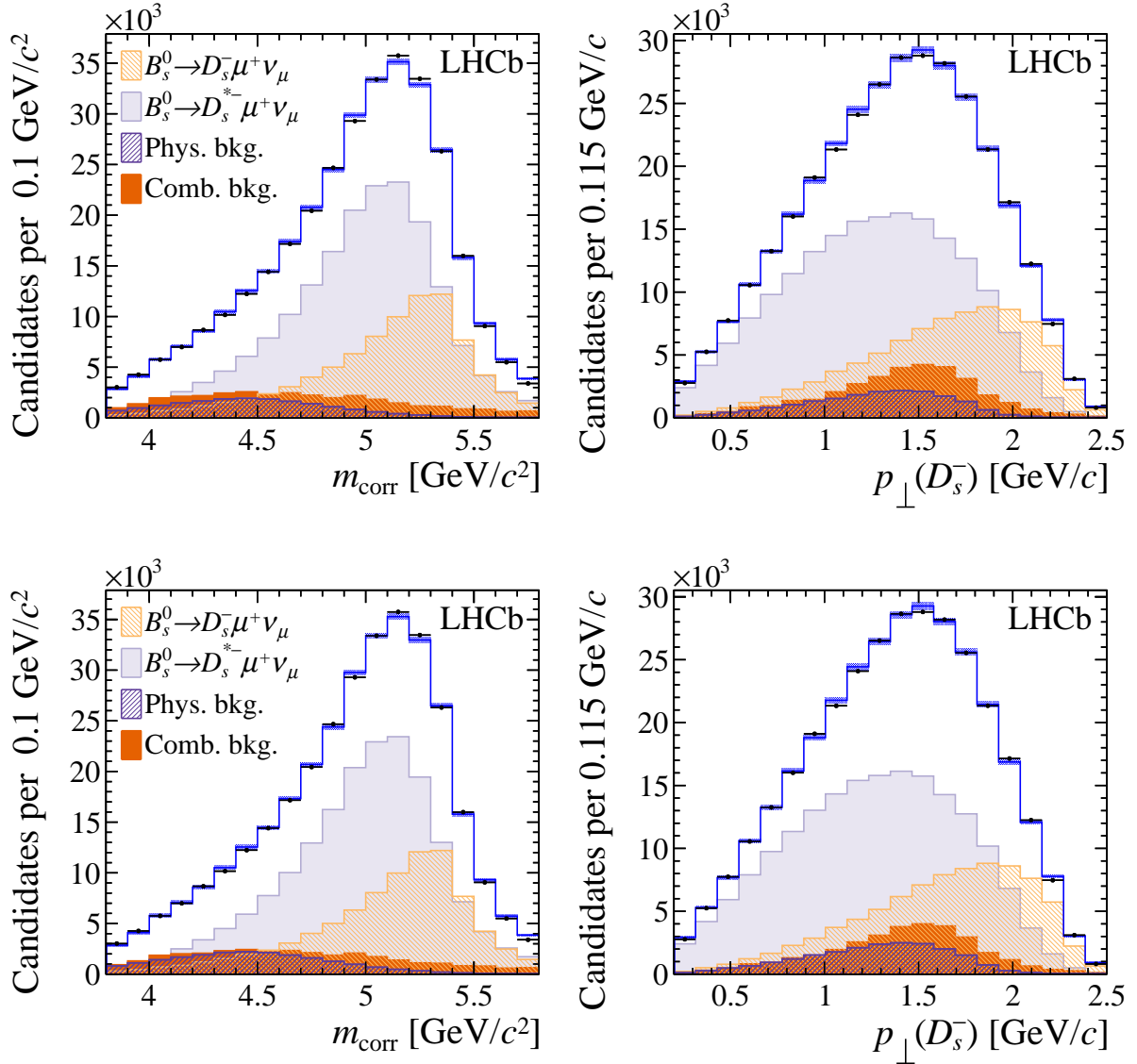
Figure 5: Distribution of (left) m_{corr} and (right) $p_\perp(D_s^-)$ for the inclusive sample of signal $D_s^-\mu^+$ candidates selected without any cut on the m_{corr}–$p_\perp(D_s^-)$ plane, with fit projections based on the (top) CLN and (bottom) BGL parametrizations overlaid. The projections of the two components due to physics background are merged together for displaying purposes.
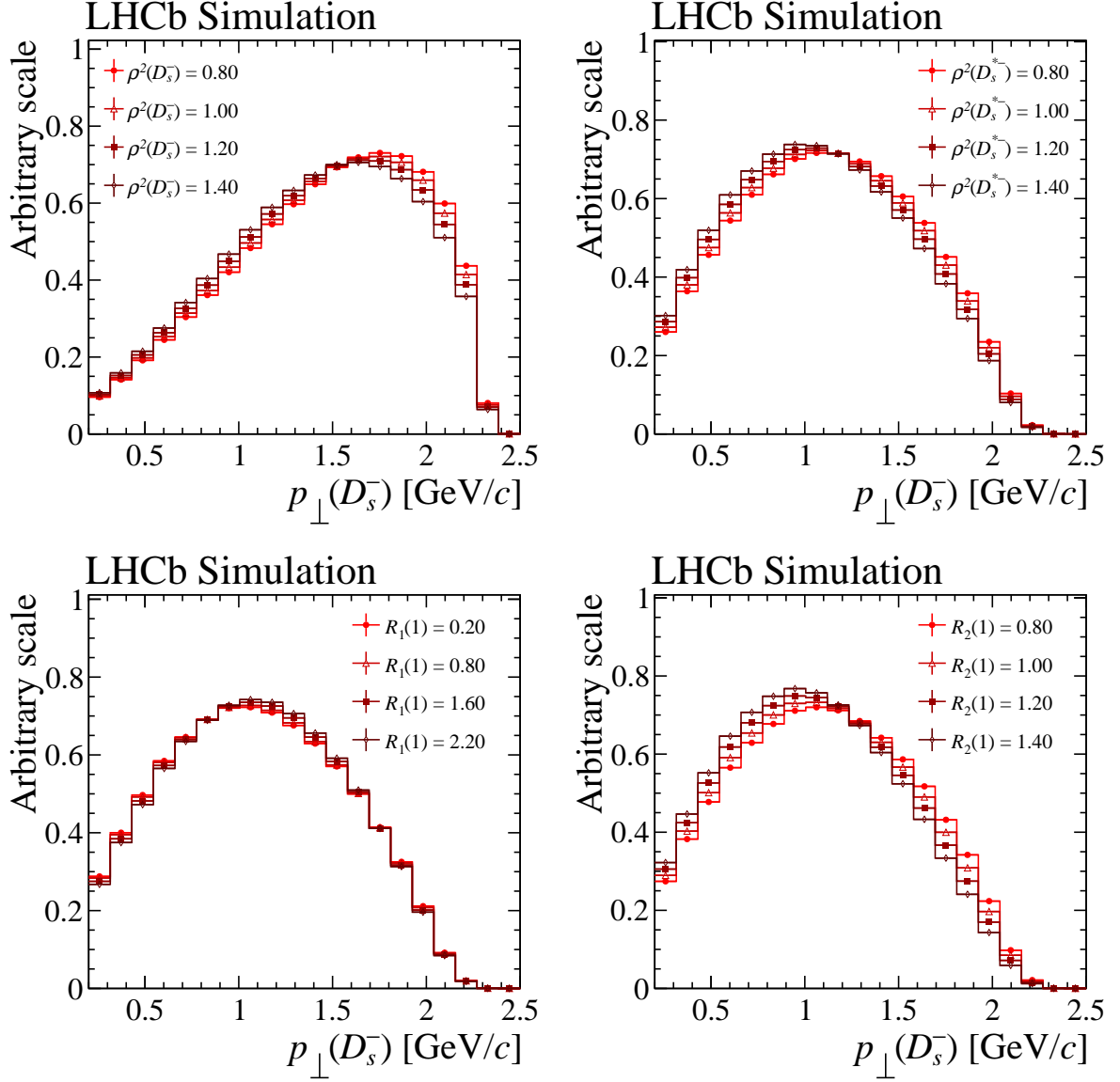
Figure 6: Comparison of the $p_\perp(D_s^-)$ distributions for $B_s^0 \to D_s^- \mu^+ \nu_\mu$ decays with different values of $\rho^2(D_s^-)$ (top left); and for $B_s^0 \to D_s^{*-} \mu^+ \nu_\mu$ decays with different values of $\rho^2(D_s^{*-})$ (top right), $R_1(1)$ (bottom left) and $R_2(1)$ (bottom right).

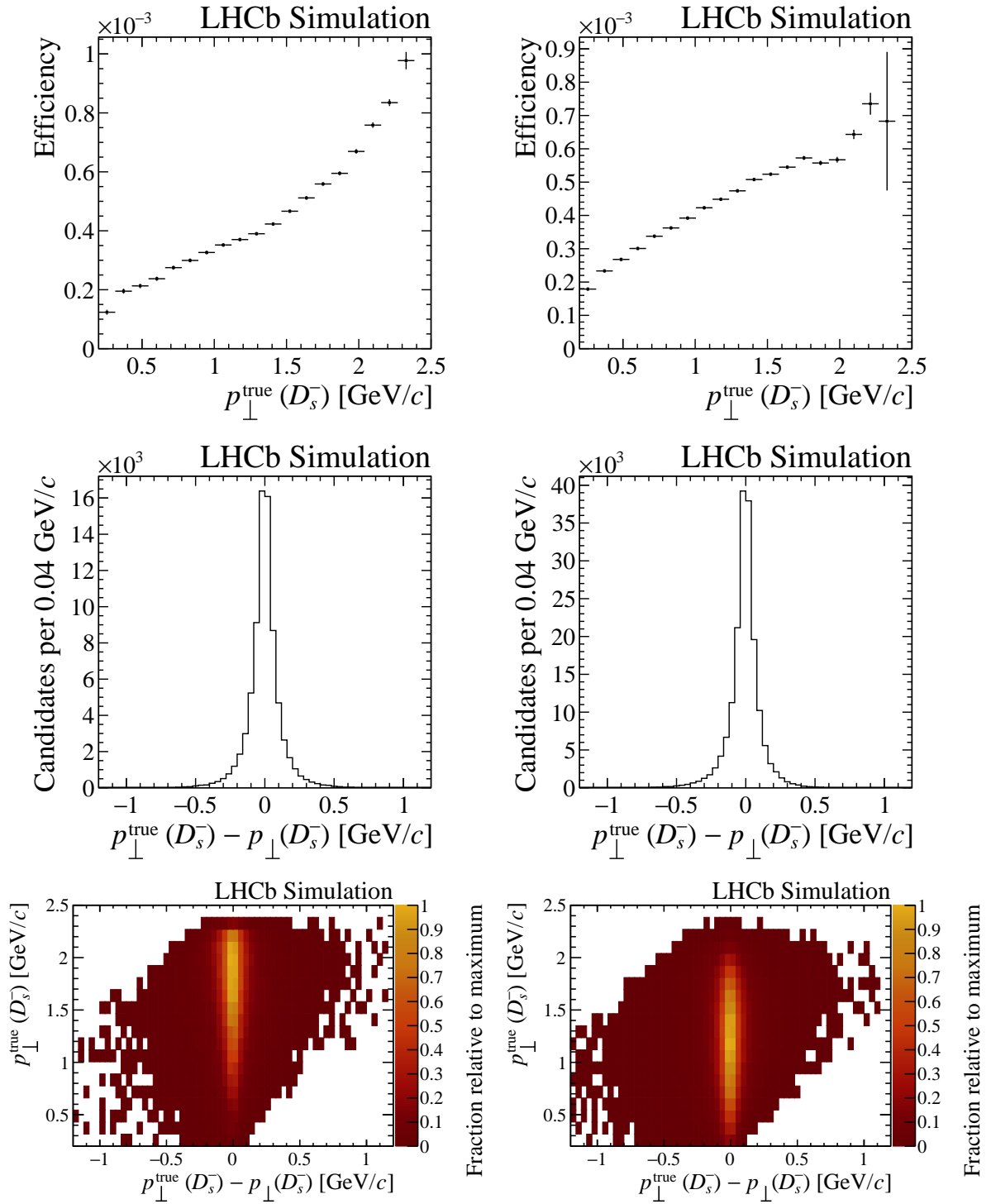Figure 7: The columns show (left) $B_s^0 \to D_s^- \mu^+ \nu_\mu$ and (right) $B_s^0 \to D_s^{*-} \mu^+ \nu_\mu$ simulated events. The rows display (top) the efficiency as a function of $p_\perp(D_s^-)$, (middle) the distribution of $p_\perp^{\text{true}}(D_s^-) - p_\perp(D_s^-)$ and (bottom) the distribution of $p_\perp^{\text{true}}(D_s^-)$ as a function of $p_\perp^{\text{true}}(D_s^-) - p_\perp(D_s^-)$. The simulated samples are weighted using the values of the form-factors obtained in the CLN parametrization.
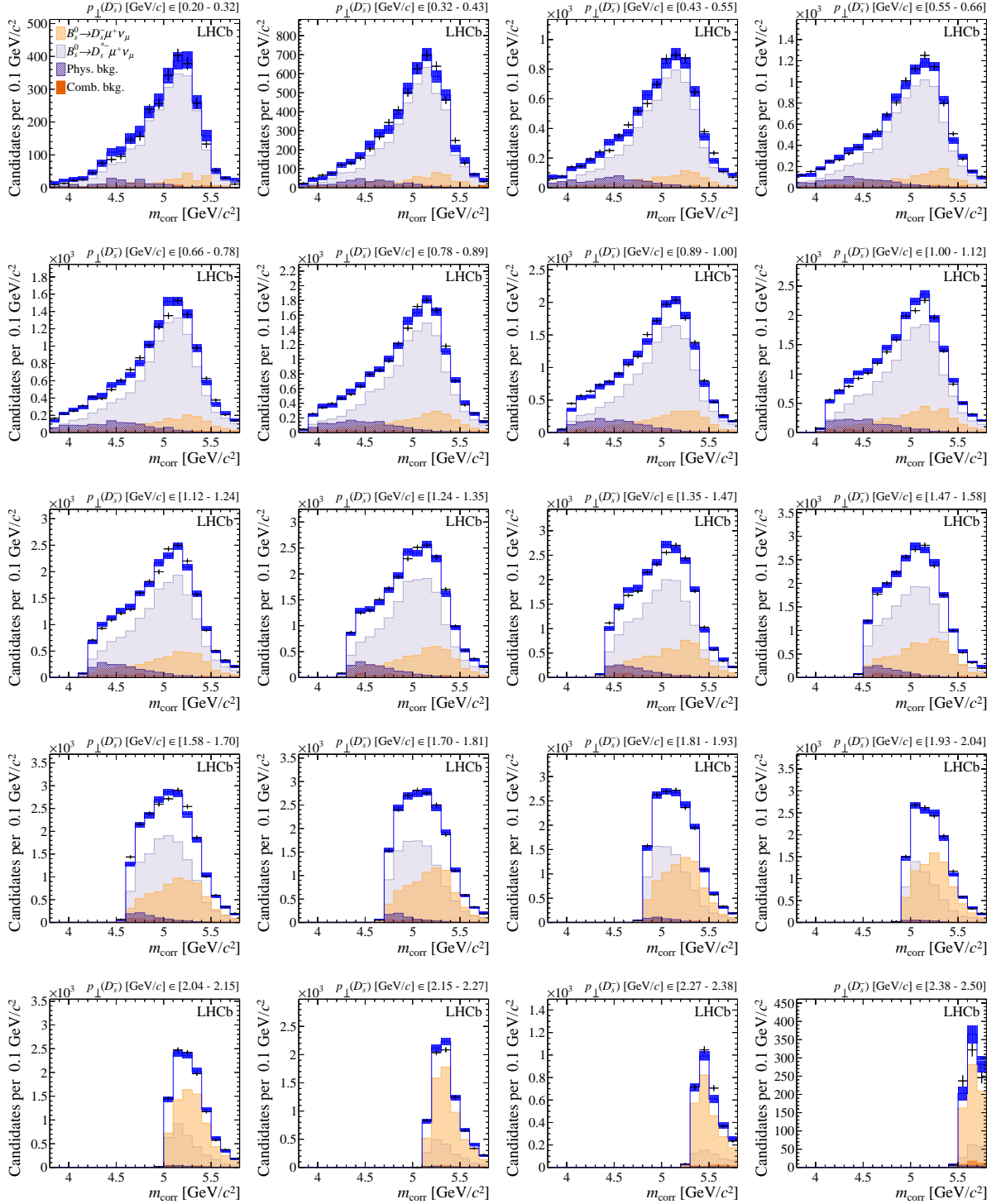
Figure 8: Distribution of $m_{\rm corr}$ in bins of $p_\perp(D_s^-)$ for the signal sample, with fit projections overlaid in the CLN parametrization. The shaded blue area represents the uncertainty on the templates.
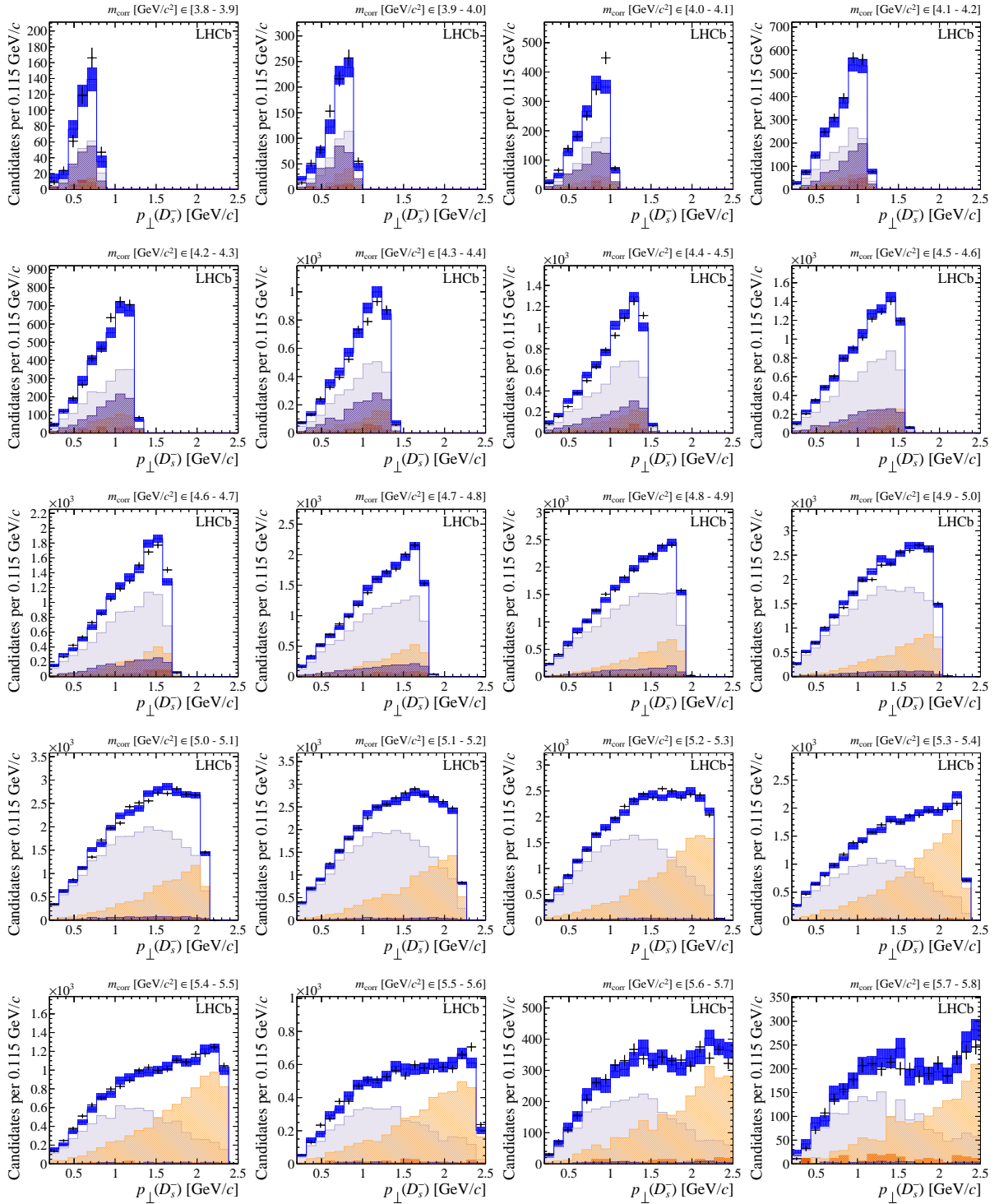
Figure 9: Distribution of $p_\perp(D_s^-)$ in bins of $m_{\rm corr}$ for the signal sample, with fit projections overlaid in the CLN parametrization. The shaded blue area represents the uncertainty on the templates.

Figure 10: Distribution of m_{corr} in bins of $p_\perp(D_s^-)$ for the signal sample, with fit projections overlaid in the BGL parametrization. The shaded blue area represents the uncertainty on the templates.
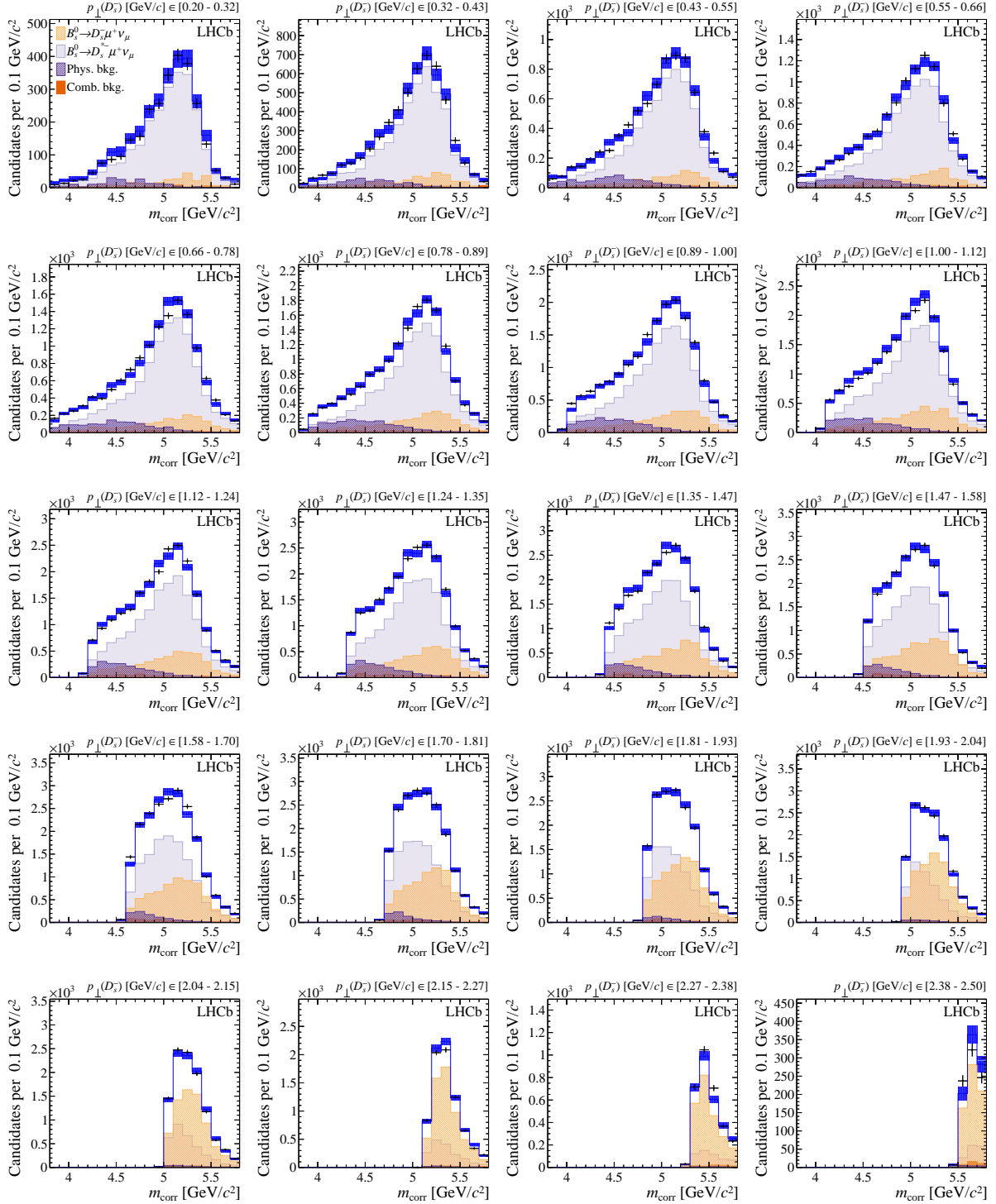
Figure 11: Distribution of $p_\perp(D_s^-)$ in bins of m_{corr} for the signal sample, with fit projections overlaid in the BGL parametrization. The shaded blue area represents t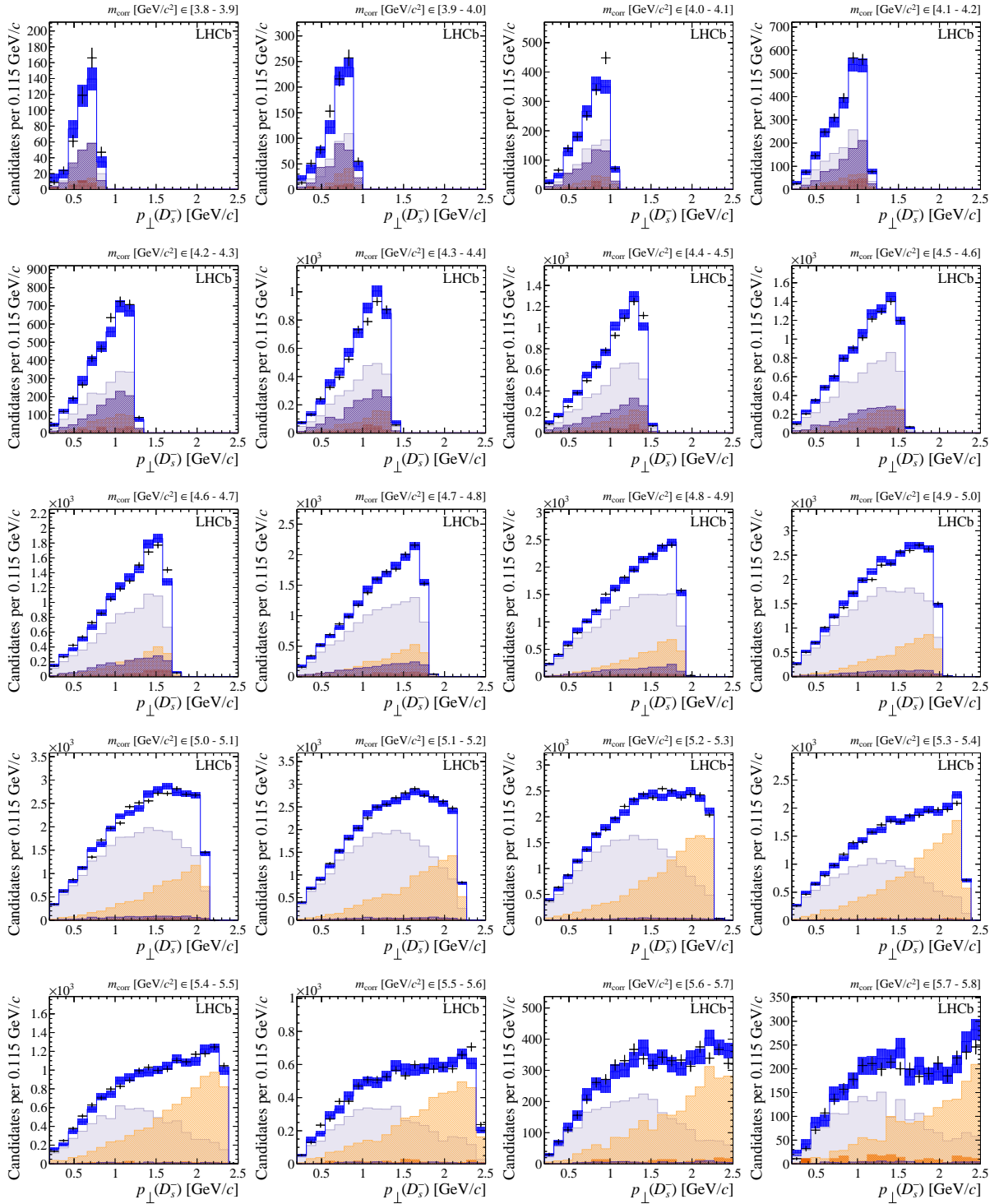he uncertainty on the templates.